Revealing the role of tin fluoride additive in narrow bandgap Pb-Sn perovskites for highly efficient flexible all-perovskite tandem cells

Johnpaul K. Pious[1],[#] Yannick Zwirner[1],[#] Huagui Lai[1],[#] Selina Olthof[2], Quentin Jeangros[3,4], Evgeniia Gilshtein[1], Radha K. Kothandaraman[1], Kerem Artuk[3], Philipp Wechsler[1], Cong Chen[5],[*] Christian M. Wolff[3], Dewei Zhao[5], Ayodhya. N. Tiwari[1], and Fan Fu[1*]

[1] Laboratory for Thin Films and Photovoltaics, Empa - Swiss Federal Laboratories for Materials Science and Technology, Dübendorf, Switzerland

[2] Department of Chemistry, University of Cologne, Greinstrasse 4–6, 50939, Cologne, Germany

[3] Photovoltaics and Thin Film Electronics Laboratory, EPFL - École Polytechnique Fédérale de Lausanne, Neuchâtel, Switzerland

[4] Sustainable Energy Center, Centre Suisse d'Electronique et de Microtechnique (CSEM), Jaquet-Droz 1, 2002 Neuchâtel, Switzerland

[5] College of Materials Science and Engineering, Engineering Research Center of Alternative Energy Materials & Devices, Ministry of Education, Sichuan University, Chengdu, Sichuan, 610065 China

[#] J.K.P., Y.Z., and H.L. contributed equally to this work.

[*] fan.fu@empa.ch; chen.cong@scu.edu.cn

Abstract

Tin fluoride (SnF_2) is an indispensable additive for high-efficiency Pb-Sn perovskite solar cells (PSCs). However, the spatial distribution of SnF_2 in the perovskite absorber is seldom investigated while essential for a comprehensive understanding of the exact role of the SnF_2 additive. Herein, we revealed the spatial distribution of SnF_2 additive and made structure-optoelectronic properties-flexible photovoltaic performance correlation. We observed the chemical transformation of SnF_2 to a fluorinated oxy-phase on the Pb-Sn perovskite film surface, due to its rapid oxidation. In addition, at the buried perovskite interface, we detected and visualized the accumulation of F^- ions. We found that the photoluminescence quantum yield of Pb-Sn perovskite reached the highest value with 10 mol% SnF_2 in the precursor solution. When integrating the optimized absorber in flexible devices, we obtained the flexible Pb-Sn perovskite narrow bandgap (1.24 eV) solar cells with an efficiency of 18.5% and demonstrated 23.1%-efficient flexible 4-terminal all-perovskite tandem cells.

Introduction

Solar cells based on perovskites with a general formula ABX₃ (A = methylammonium (MA⁺), formamidinium (FA⁺), and Cs⁺; B = Pb^{2+}, Sn^{2+}; X = Cl⁻, Br⁻, and I⁻) have shown rapid performance advancement, now reaching a certified power conversion efficiency (PCE) of 25.7%.[1] Further improvement in the efficiency of single junction perovskite solar cells (PSCs) will be restricted by the Shockley-Queisser limit.[2] Stacking two perovskite absorbers with complementary bandgaps in all-perovskite tandem solar cells (TSCs) holds great promise to go beyond the Shockley-Queisser efficiency limit of single-junction PSCs.[3-5]

Flexible all-perovskite TSC is an emerging field of research owing to its flexible and lightweight attributes, making them attractive for wearable electronics, avionics, building- and mobility-integrated photovoltaics.[6,7] In addition, the low-temperature solution processability of perovskites makes it viable for high throughput roll-to-roll (R2R) manufacturing, with the potential to substantially reduce the production cost and CO_2 footprint. Despite that, little progress has been made in this field, with only two publications reporting PCE of 21.3% and 24.4% for two-terminal (2T) flexible all-perovskite TSCs.[8,9] These values are well below the highest reported values for their rigid counterparts on 2-terminal (2T, 28.0%) and four-terminal (4T, 25.4%) tandem configuration, respectively.[10,11] So far there is no report on 4T all-perovskite tandem cells based on flexible substrates. Flexible foils pose several obstacles due to low thermal tolerance, high roughness, and poor wettability. Apart from that, it has proven difficult to grow homogenous narrow bandgap Pb-Sn perovskite films on flexible substrates owing to their fast crystallization.[12,13] Sn vacancy defect formation and its detrimental consequences in Pb-Sn perovskites are cause for concern, which becomes more severe when the concentration of Sn exceeds 50 mol% in the metal site.[14-18]

Tin fluoride (SnF_2) is an indispensable additive in the Pb-Sn perovskite precursor solution to suppress the oxidation of Sn^{2+} ions. Previously, various groups have added different amounts of SnF_2 (5 mol% - 30 mol% relative to SnI_2) to fabricate Pb-Sn PSCs, but there is no consensus as to the optimal amount of SnF_2 needed, nor was the spatial distribution comprehensively investigated.[19-22] Furthermore, there are several competing explanations detailing the effects of SnF_2 as an additive on the crystal structure and local chemical environment in Pb-Sn perovskites. For instance, Zhao et al. proposed that SnF_2 fills the Sn vacancies and expands the perovskite lattice, which subsequently shifts the XRD peaks to a lower angle.[23] On the contrary, Herz and co-workers observed a lattice shrinkage and associated XRD peak shift to higher 2θ upon increasing the SnF_2 concentration; which was attributed to the Sn doping in the perovskite lattice.[24] The aforementioned reports imply that the spatial location or distribution of SnF_2 in the Pb-Sn perovskite film is not yet fully understood. In-depth understanding of the role of SnF_2 on the phase-composition, microstructure, and optoelectronic properties of Pb-Sn perovskite thin films as well as its spatial distribution require further investigation to improve the efficiency and stability of Pb-Sn PSCs.

In this work, we varied the SnF_2 concentration added to the $(FASnI_3)_{0.6}(MAPbI_3)_{0.4}$ perovskite precursor to systematically investigate its effects on the film morphology, crystal structure, optoelectronic properties, and flexible solar cell device performance. We unraveled that SnF_2 addition modulates the perovskite grain topography and suppresses the defect formation via a p-type self-doping mechanism. SnF_2 segregates both at the hole transport layer/perovskite and electron transport layer/perovskite interfaces. We observe the formation of fluorinated tin dioxide at the top surface of the $(FASnI_3)_{0.6}(MAPbI_3)_{0.4}$ films. Although SnF_2 improved the optoelectronic quality of the Pb-Sn absorber, beyond a threshold of 10% further addition of SnF_2 impairs the device performance through a lowering of the FF and V_{OC}. As a result of the optimized SnF_2 supplementation, we achieved flexible narrow bandgap PSC with a champion efficiency of 18.5%. Furthermore, we demonstrated over 23% flexible 4-terminal all perovskite tandem solar cell combining a 1.24 eV Pb-Sn bottom subcell and a 1.78 eV perovskite top cell.

Results and Discussion

$(FASnI_3)_{0.6}(MAPbI_3)_{0.4}$ perovskite thin films with different mol% of SnF_2 additive in the precursor solution were deposited using an anti-solvent assisted method as described in the experimental section. The scanning electron microscopy (SEM) images of perovskite films deposited on PEN/ITO/PEDOT:PSS substrate showed smooth morphology up to 2.5mol% SnF_2 (**Figures** 1a and b), while a further increase in concentration resulted in surface texture. For samples with 5mol% SnF_2, terraces-like structures start to appear as shown in the SEM (**Figure** 1c) and atomic force microscopy (AFM) images (**Figure** S1). These films exhibited a high root mean square roughness (R_q) value of 36.7 compared to control samples without SnF_2 ($R_q = 29.6$).
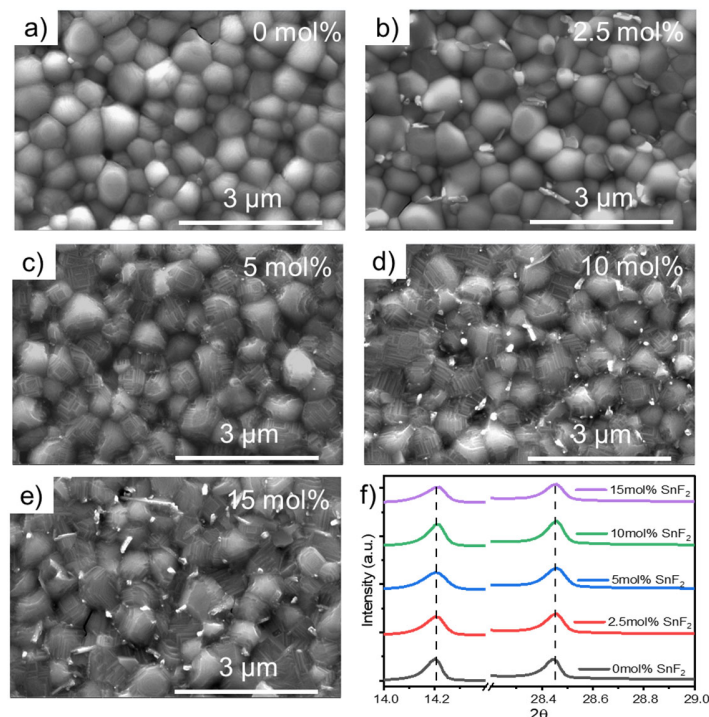
Figure 1. a) – e) SEM surface morphology of Pb-Sn perovskite films with different mol% of SnF_2 additive. f) XRD patterns of the perovskite films with various amounts of SnF_2.

Thin films with 10mol% and 15mol% SnF_2 content exhibited "white spots" in the SEM images (**Figures** 1d and e). We believe that the textured features on the perovskite grain surfaces might have originated from the modulated colloidal property of the perovskite precursor solution. This could be ascribed to the $[SnI_x]^{2-x}$ adduct formation as a result of SnF_2 complexation with Sn^{4+} ions as reported previously.[25]

To understand the role of SnF_2 on the crystal structure of the Pb-Sn perovskite, the XRD patterns of the perovskite films with various amounts of SnF_2 were analyzed. Preferential orientation of Pb-Sn perovskite crystallites along the (110) and (220) lattice planes was observed (**Figure** 1f). The perovskite films retained a similar crystallinity up to 15mol% SnF_2 addition as indicated by their similar diffraction peak intensity. There was no noticeable XRD peak shift upon increasing the SnF_2 concentration up to 15 mol%. Previous reports proposing the Sn vacancy filling and metal site doping during SnF_2 supplementation showed XRD peak shifts to lower or higher 2θ values, respectively.[19, 23] However, our XRD measurements suggest that SnF_2 does not alter the perovskite lattice.

Element	C	N	O	F	Sn	I	Pb
Atom %	17.3	28.4	22.3	3.6	3.8	21.0	3.6
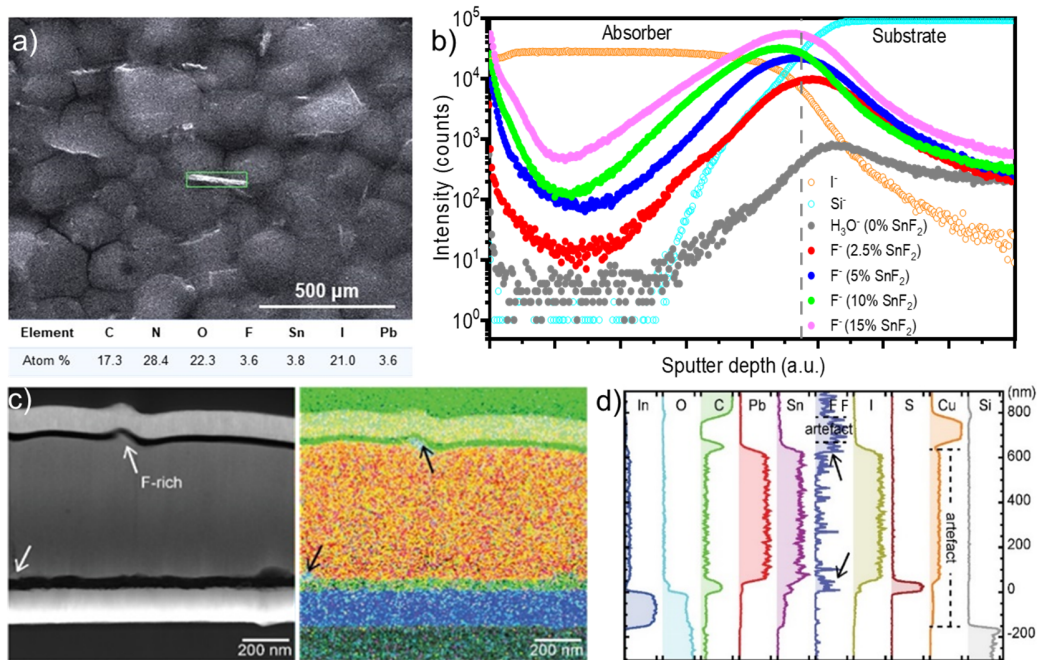
Figure 2. a) Scanning electron microscopy (SEM) image and energy dispersive X-ray (EDX) elemental analysis of $(FASnI_3)_{0.6}(MAPbI_3)_{0.4}$ thin film with 10mol% SnF_2. The chemical composition in the area of white aggregate (green rectangular box) is shown in the table. b) ToF-SIMS depth profiles of $(FASnI_3)_{0.6}(MAPbI_3)_{0.4}$ perovskite thin films with different concentrations of SnF_2. c) Cross-sectional scanning transmission electron microscopy high-angle annular dark-field (STEM HAADF) image with the corresponding EDX mapping and (d) EDX line profiles for the flexible Pb-Sn perovskite solar cell. Arrows indicate the fluoride-rich regions at the top and bottom interfaces of perovskite with transport layers.

To investigate the composition of the white spots observed in the SEM images, we performed an EDX analysis and identified the presence of fluorine, which hinted at the presence of SnF_2 (**Figure** 2 a). Even though it is important to understand the distribution of SnF_2 in the perovskite film to explicitly unravel the role of SnF_2 additive, so far only a little research attention was paid in this direction. To shed light on this missing knowledge, we performed the time-of-flight secondary ion mass spectrometry (ToF-SIMS) depth profiling measurements on perovskite/glass layer stacks. The marker F^- secondary ion signal representing SnF_2 was detected throughout the film, with a higher signal strength both at the top and bottom interfaces of the perovskite absorber, irrespective of the concentration. At low concentrations of SnF_2 (2.5 mol% and 5 mol%), F^- ions appear to preferentially segregate at the buried perovskite/HTL interface. At higher SnF_2 supplementation, the top surface of the perovskite layers has shown F^- ion signal intensity on par with the bottom interface (**Figure** 2 b). Generally, the summed F^- ion signal throughout the layer increases with an increase in the amount of SnF_2 in the perovskite precursor solution. To further visualize the spatial distribution of SnF_2, we conducted cross-sectional EDX mapping using HAADF-STEM. The EDX mapping of full device stacks with 10mol% SnF_2 confirms the accumulation of SnF_2 both at the perovskite/HTL and perovskite/ETL interfaces (**Figure** 2 c).
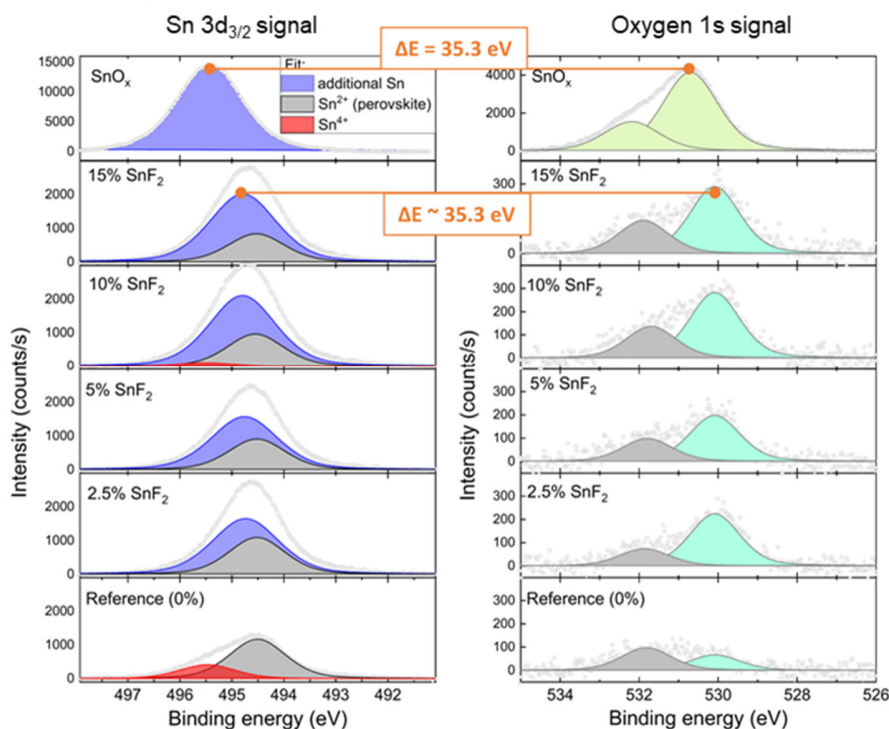
Figure 3. XPS core level spectra of Sn3d$_{3/2}$ and O1s of SnO_2 as well as the Pb-Sn perovskite films with varied amounts of SnF_2 additive.

X-ray photoelectron spectroscopy (XPS) was performed to study in detail the composition of the surfaces after the addition of different amounts of SnF_2 and to analyze the element oxidation states. The Sn3d$_{3/2}$ signal is shown on the left side of **Figure** 3. Fitting this feature is rather challenging since Sn can show up at different binding energies. Possible chemical environments are intact perovskite (Sn^{+2}), degraded Sn^{+4} phases, intact SnF_2 domains, or even new species, as will be

revealed below. The rigorous fitting procedure is detailed in the Supporting Information and the resulting features are indicated in **Figure** 3. For the perovskite film without SnF_2 additive, a clear signal originating from Sn^{+4} is seen as marked by the red peak at higher binding energy, in addition to the perovskite-related signal (grey). Once SnF_2 is added, another rather intense Sn signal appears, marked in blue, with binding energy in between the ones observed for Sn^{+2} and Sn^{+4}. This additional peak makes overlaps with the Sn^{4+} signal, reducing the ability to quantify the latter. Even though the fits are less robust, our analysis indicates that the amount of Sn^{+4} is likely negligible in the SnF_2-containing samples.

Also, the F1s core level signal was analyzed upon adding SnF_2 to the perovskite precursor solution, which confirms the presence of fluorine on the surface of the perovskite layer (**Figure** S2). To determine whether the fluorine is still bound to Sn, we analyzed also a pure SnF_2 film which is included in **Figure** S2. Notably, the binding energy difference between F1s and $Sn3d_{3/2}$ signals in pure SnF_2 ($\Delta E=188.67$ eV) does not match the one observed for F1s and the newly emerged blue Sn feature ($\Delta E=189.29$ eV). This suggests the formation of a new chemical species. A second indication that the additional Sn is not (exclusively) bound to fluorine comes from the analysis of the relative concertation of the elements which is SnF_x (x = 0.2 – 0.5), meaning that there is a severe lack of F signal.

Interestingly, SnF_2 supplementation resulted in the appearance of an oxygen O1s signal at lower binding energy with high intensity compared to the reference sample without SnF_2, see Figure 3 on the right. From these observations, we hypothesized the new species formed to be fluorinated SnO_2 because SnF_2 on the exposed perovskite surface can be readily oxidized in presence of oxygen and hence serve as an oxygen scavenger to hinder the degradation of the absorber. To further confirm this, we compared the binding energy difference (ΔE) of Sn ($3d_{3/2}$) and O (1s) signals from a pure SnO_2 sample (**Figure** 3 top) with that in the Pb-Sn perovskite films. The $Sn3d_{3/2}$ vs.O1s core level difference in this SnO_2 sample is $\Delta E = 35.28$ eV, which matches with the ones observed in the perovskite absorbers ($\Delta E = 35.31 \pm 0.03$ eV) validating the formation of fluorinated SnO_2 on the surface of the perovskite layer. From the fitted XPS data of the perovskite films with different concentrations of SnF_2, we estimated the composition of the newly formed inorganic species as SnO_yF_x (x = 0.2 – 0.5, y = 0.9 - 1.7).

The effect of the SnF_2 additive on the optoelectronic quality of Pb-Sn perovskites supplemented with different amounts of SnF_2 was examined using photoluminescence quantum yield (PLQY) measurements (**Figure** 4a). Since the charge extraction layers are known to introduce additional nonradiative recombination, glass/PEDOT:PSS/$(FASnI_3)_{0.6}(MAPbI_3)_{0.4}$/$C_{60}$ stacks were used for the PLQY measurements to ensure a reliable correlation with the actual device performance. The PLQY values showed an increasing trend up to 10 mol% SnF_2 addition and then decreased at higher SnF_2 concentration (15 mol%). This trend could be attributed to the improved suppression of Sn oxidation up to 10 mol% SnF_2 addition in the precursor solution, and then roughly stagnates. This is in line with a reduction of nonradiative bulk recombination due to reduced oxidation during and after crystallization and in addition a reduction of interfacial recombination due to the formation of F-enriched phases at both interfaces. Therefore, the optimal concentration of SnF_2 additive to minimize the non-radiative recombination in $(FASnI_3)_{0.6}(MAPbI_3)_{0.4}$ based PSC devices would be 10 mol%. In line with the above observation, ultraviolet photoelectron

spectroscopy analysis showed a notable suppression of states close to the Fermi level when SnF_2 was introduced into the perovskite films; these are likely related to gap states tailing into the band gap (**Figure** S3). This could be attributed to the reduction of detrimental p-type self-doping in Pb-Sn perovskite films supplemented with SnF_2. To verify the hypothesis of SnF_2-mediated defect healing and to investigate the role of SnF_2 on PV performance, we have fabricated Pb-Sn (NBG) PSCs on flexible substrates.
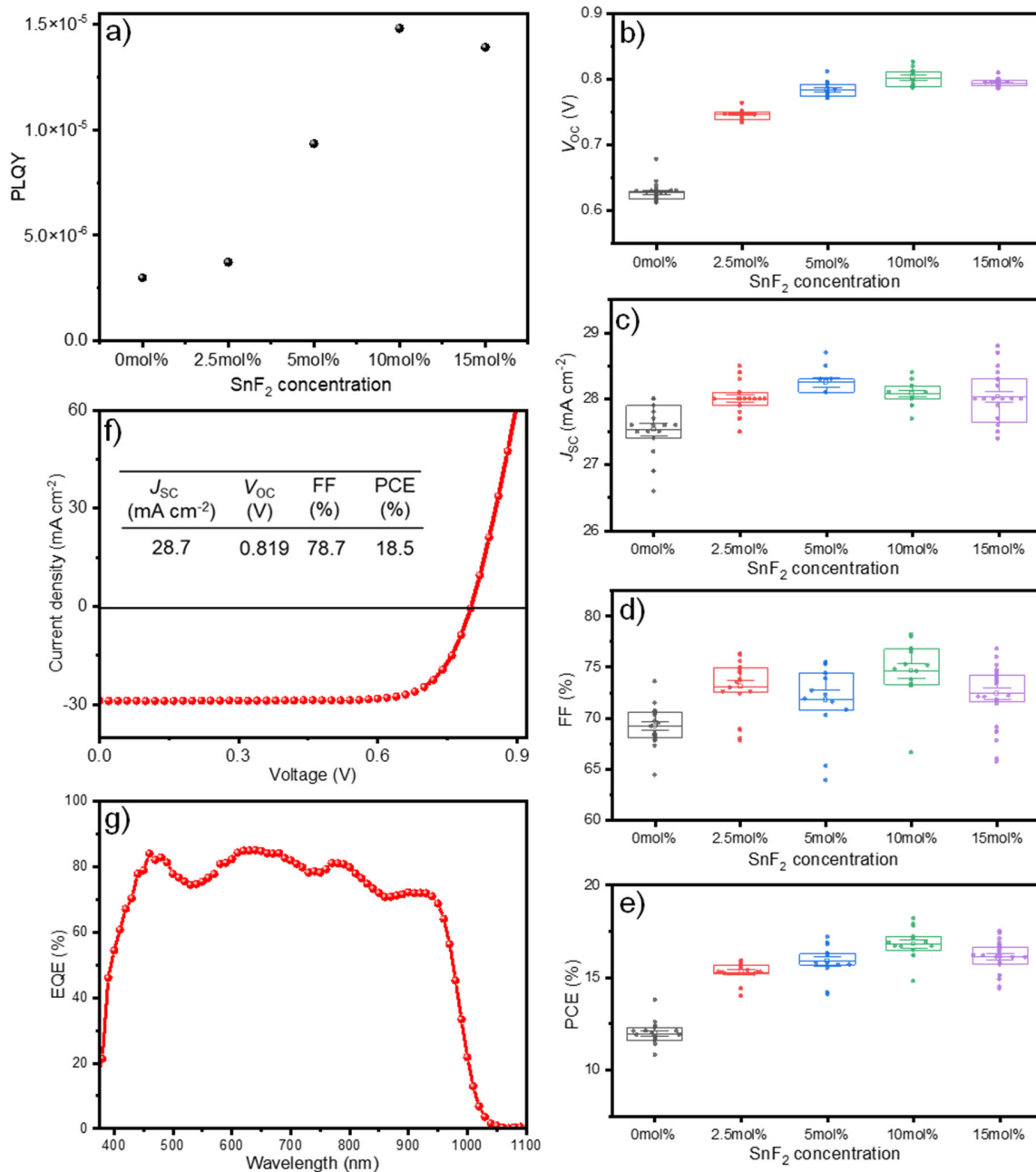

Figure 4. a) Photoluminescence quantum yield of the perovskite absorber with different amounts of SnF_2 additive sandwiched between the charge extraction layers (HTL and ETL). The box chart shows the variation in Pb-Sn PSC parameters such as b) V_{OC}, c) J_{SC}, d) FF, and e) PCE with

different mol% of SnF$_2$ additive. f) and g) are *J-V* and EQE plots of the champion flexible NBG device.

The *J-V* parameters of the flexible NBG PSCs fabricated with different SnF$_2$ additive concentrations are summarized in **Figure** 4b-e. The box plot shows a clear trend of open-circuit voltage (V_{OC}) improvement upon increasing the amount of SnF$_2$ up to 10 mol% reaching a maximum average value of 810 mV. For higher SnF$_2$ concentrations (15 mol%), the average value of V_{OC} is slightly decreased (**Figure** 4b). The average value of fill factor (FF) increased up to 10mol% SnF$_2$ supplementation, implying an improved intimate contact between perovskite and charge selective contacts (**Figure** 4d). The drop in the average value of FF above 10 mol% SnF$_2$ might be due to the excess SnF$_2$ aggregation at the front and rear interfaces of the perovskite absorber. The V_{OC} of (FASnI$_3$)$_{0.6}$(MAPbI$_3$)$_{0.4}$ based devices showed a similar trend (**Figure** 4e) as that of the PLQY data, implying that the SnF$_2$ additive improves the optoelectronic quality of the absorber, but also the whole stack. As a result, the flexible NBG PSC with 10 mol% SnF$_2$ exhibited the optimal performance with a champion efficiency of 18.5%, corresponding to a V_{OC} of 0.819 V, a J_{SC} of 28.7 mA cm^{-2}, and FF of 78.7% (**Figure** 4f). The device delivered a steady-state efficiency of 18.2% during maximum power point tracking (**Figure** S4). The integrated J_{SC} value of 28.5 mA cm^{-2} obtained from the EQE spectrum (**Figure** 4g) is in good agreement with the J_{SC} value determined from the *J-V* measurement.

To verify the potential of our flexible Pb-Sn PSCs in the application of all-perovskite TSCs, we mechanically stacked the champion flexible Pb-Sn PSC with the flexible wide bandgap PSC developed in our lab and demonstrate a 4T flexible all-perovskite TSC as shown in **Figure** 5a. The best performing flexible 4T all-perovskite TSC fabricated using a 1.24 eV Pb-Sn bottom subcell and a 1.78 eV Cs$_{0.12}$FA$_{0.8}$MA$_{0.08}$PbI$_{1.8}$Br$_{1.2}$ top subcell delivered a PCE of 23.1% (**Figure** 5b). The integrated J_{SC} values obtained from EQE spectra for the WBG top cell and NBG bottom cell are 15.46 and 12.45 mA cm^{-2}, respectively (**Figure** 5c). To the best of our knowledge, this is the first report of flexible Pb-Sn NBG (1.24 eV) single junction and flexible 4T all-perovskite TSCs (**Figure** 5d).[8,9,26]
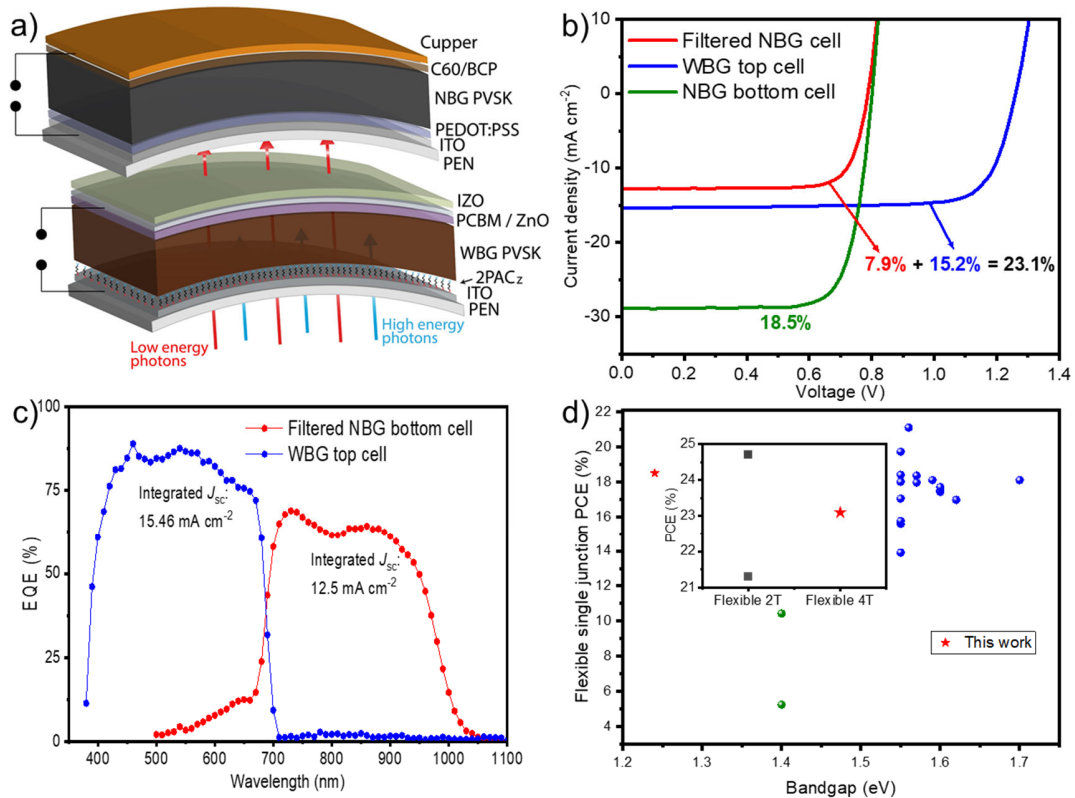
Figure 5. a) Schematic of a flexible 4T all-perovskite TSC. b) and c) are *J-V* and EQE characteristics of individual subcells in the 4T tandem configuration. d) Plot of reported flexible single junction PSCs efficiencies versus bandgap. The inset graph shows the reported flexible all-perovskite TSC efficiencies. Red asterisks represent the PCE values of our devices presented in this work.

Conclusion

In conclusion, we unraveled that the addition of SnF_2 to the precursor ink induces a textured morphology in the Pb-Sn perovskite films, and the F^- ions from SnF_2 segregate both at the top and bottom interfaces of the perovskite layer. Employing STEM, we have visualized the presence of F^- ions islands at the perovskite/HTL and perovskite/ETL interfaces. We observed that the SnF_2 present on the exposed perovskite surface is easily oxidized resulting in the formation of $SnO_{1.2}F_{(0.2-0.5)}$. Although SnF_2 doesn't have any noticeable impact on the perovskite crystal structure, electronic defects at the valence band edge states are reduced, reducing recombination and hence allowing an increase in the quasi Femi-level splitting of the absorber. Excess SnF_2 does not further improve the V_{OC} of the NBG PSCs, but results in a mildly reduced fill factor and performance. By carefully optimizing the concentration of SnF_2, we achieved a flexible NBG single-junction PSC efficiency of up to 18.5% and a 4-T tandem efficiency of 23.1%. Our comprehensive experimental investigation including surface and depth elemental profiling techniques in combination with the device performance evaluation unveiled the multiple unknown roles of SnF_2 additive and a new fluorinated tin oxide ($SnO_{1.2}F_{(0.2-0.5)}$) based interface formation in Pb-Sn PSCs.

ASSOCIATED CONTENT

Supporting Information

Experimental details, AFM images, XPS and UPS spectra, and MPP stability tracking data.

AUTHOR INFORMATION

Notes

The authors declare no competing financial interest.

References

1. Best Research-Cell Efficiency Chart; https://www.nrel.gov/pv/cell-efficiency.html (2021), Accessed 8th June 2022
2. Kothandaraman, R. K.; Jiang, Y.; Feurer, T.; Tiwari, A. N.; Fu, F. Near-Infrared-Transparent Perovskite Solar Cells and Perovskite-Based Tandem Photovoltaics. *Small Methods* **2020**, *4*, 2000395.
3. Leijtens, T.; Bush, K. A.; Prasanna, R.; McGehee, M. D. Opportunities and challenges for tandem solar cells using metal halide perovskite semiconductors. *Nat. Energy* **2018** 828–838.
4. Wang, Y.; Zhang, M.; Xiao, K.; Lin, R.; Luo, X.; Han, Q.; Tan, H. Recent progress in developing efficient monolithic all-perovskite tandem solar cells. *J. Semicond.* **2020**, *41*, 051201.

5. Zheng, X.; Alsalloum, A. Y.; Hou, Y.; Sargent, E. H.; Bakr, O. M. All-Perovskite Tandem Solar Cells: A Roadmap to Uniting High Efficiency with High Stability. *Acc. Mater. Res.* **2020**, *1*, 63−76.

6. Gao, Y.; Huang, K.; Long, C.; Ding, Y.; Chang, J.; Zhang, D.; Etgar, L.; Liu, M.; Zhang, J.; Yang, J. Flexible Perovskite Solar Cells: From Materials and Device Architectures to Applications. *ACS Energy Lett.* **2022**, *7*, 1412−1445.

7. Zhang, J.; Zhang, W.; Cheng, H.-M.; Silva, S. R. P. Critical Review of Recent Progress of Flexible Perovskite Solar Cells. *Mater. Today* **2020**, *39*, 66−88.

8. Palmstrom, A. F.; Eperon, G. E.; Leijtens, T.; Prasanna, R.; Habisreutinger, S. N.; Nemeth, W.; Gaulding, E. A.; Dunfield, S. P.; Reese, M.; Nanayakkara, S.; Moot, T.; Werner, J. M.; Liu, J.; To, B.; Christensen, S. T.; McGehee, M. D.; van Hest, M. F.A.M.; Luther, J. M.; Berry, J. J.; Moore, D. T. Enabling Flexible All-Perovskite Tandem Solar Cells. *Joule* **2019**, 2193–2204.

9. Li, L.; Wang, Y.; Wang, X.; Lin, R.; Luo, X.; Liu, Z.; Zhou, K.; Xiong, S.; Bao, Q.; Chen, G.; Tian, Y.; Deng, Y.; Xiao, K.; Wu, J.; Saidaminov, M. I.; Lin, H.; Ma, C.-Q.; Zhao, Z.; Wu, Y.; Zhang, L.; Tan, H. Flexible all-perovskite tandem solar cells approaching 25% efficiency with molecule-bridged hole-selective contact. *Nat. Energy* **2022**, https://doi.org/10.1038/s41560-022-01045-2.

10. Tong, J.; Song, Z.; Kim, D. H.; Chen, X.; Chen, C.; Palmstrom, A. F.; Ndione, P. F.; Reese, M. O.; Dunfield, S. P.; Reid, O. G.; Liu, J.; Zhang, F.; Harvey, S. P.; Li, Z.; Christensen, S. T.; Teeter, G.; Zhao, D.; Al-Jassim, M. M.; van Hest, M. F. A. M.; Beard, M. C.; Shaheen, S. E.; Berry, J. J.; Yan, Y.; Zhu, K. Carrier lifetimes of >1 μs in Sn-Pb perovskites enable efficient all-perovskite tandem solar cells. *Science* **2019**, *364*, 475–479.

11. Lin, R.; Xu, J.; Wei, M.; Wang, Y.; Qin, Z.; Liu, Z.; Wu, J.; Xiao, K.; Chen, B.; Park, S. M.; Chen, G.; Atapattu, H. R.; Graham, K. R.; Xu, J.; Zhu, J.; Li, L.; Zhang, C.; Sargent, E. H.; Tan, H. All-perovskite tandem solar cells with improved grain surface passivation. *Nature* **2022**, *603*, 73–78.

12. Hu, Y.; Niu, T.; Liu, Y.; Zhou, Y.; Xia, Y.; Ran, C.; Wu, Z.; Song, L.; Müller- Buschbaum, P. Chen, Y.; Huang, W. Flexible Perovskite Solar Cells with High Power-Per-Weight: Progress, Application, and Perspectives. *ACS Energy Lett.* **2021**, *6*, 2917−2943.

13. Liu, H.; Wang, L.; Li, R.; Shi, B.; Wang, P.; Zhao, Y.; Zhang, X. Modulated Crystallization and Reduced V_{OC} Deficit of Mixed Lead−Tin Perovskite Solar Cells with Antioxidant Caffeic Acid. *ACS Energy Lett.* **2021**, *6*, 2907−2916.

14. Ghimire, N.; Bobba, R. S.; Gurung, A.; Reza, K. M.; Laskar, M. A. R.; Lamsal, B. S.; Emshadi, K.; Pathak, R.; Afroz, M. A.; Chowdhury, A. H.; Chen, K.; Bahrami, B.; Rahman, S. I.; Pokharel, J.; Baniya, A.; Rahman, M. T.; Zhou, Y.; Qiao, Q. Mitigating Open-Circuit Voltage Loss in Pb−Sn Low-Bandgap Perovskite Solar Cells via Additive Engineering. *ACS Appl. Energy Mater.* **2021**, *4*, 1731−1742.

15. Kapil, G.; Bessho, T.; Sanehira, Y.; Sahamir, S. R.; Chen, M.; Baranwal, A. K.; Liu, D.; Sono, Y.; Hirotani, D.; Nomura, D.; Nishimura, K.; Kamarudin, M. A.; Shen, Q.; Segawa, H.; Hayase, S. Tin-Lead Perovskite Solar Cells Fabricated on Hole Selective Monolayers. *ACS Energy Lett.* **2022**, *7*, 966−974.

16. Lin, R.; Xiao, K.; Qin, Z.; Han, Q.; Zhang, C.; Wei, M.; Saidaminov, M. I.; Gao, Y.; Xu, J.; Xiao, M.; Li, A.; Zhu, J.; Sargent, E. H.; Tan, H. Monolithic all-perovskite tandem solar cells with 24.8% efficiency exploiting comproportionation to suppress Sn(II) oxidation in precursor ink. *Nat. Energy* **2019**, *4*, 864–873.

17. Xiao, K.; Lin, R.; Han, Q.; Hou, Y.; Qin, Z.; Nguyen, H. T.; Wen, J.; Wei, M.; Yeddu,V.; Saidaminov, M. I.; Gao, Y.; Luo, X.; Wang, Y.; Gao, H.; Zhang, C.; Xu, J.; Zhu, J.; Sargent, E. H.; Tan, H. All-perovskite tandem solar cells with 24.2% certified efficiency and area over 1 cm^2 using surface-anchoring zwitterionic antioxidant. *Nat. Energy* **2020**, *5*, 870–880.

18. Hu, S.; Otsuka, K.; Murdey, R.; Nakamura, T.; Truong, M. A.; Yamada, T.; Handa, T.; Matsuda, K.; Nakano, K.; Sato, A.; Marumoto, K.; Tajima, K.; Kanemitsu, Y.; Wakamiya, A. Optimized Carrier Extraction at Interfaces for 23.6% Efficient Tin–Lead Perovskite Solar Cells. *Energy Environ. Sci*. **2022**, *15*, 2096–2107.

19. Ke, W.; Chen, C.; Spanopoulos, I.; Mao, L.; Hadar, I.; Li, X.; Hoffman, J. M.; Song, Z.; Yan, Y.; Kanatzidis, M. G. Narrow-Bandgap Mixed Lead/Tin-Based 2D Dion-Jacobson Perovskites Boost the Performance of Solar Cells. *J. Am. Chem. Soc*. **2020**, *142*, 15049−15057.

20. Tsai, C.-M.; Wu, H.-P.; Chang, S.-T.; Huang, C.-F.; Wang, C.-H.; Narra, S.; Yang, Y.-W.; Wang, C.-L.; Hung, C.-H.; Diau, E. W.-G. Role of Tin Chloride in Tin-Rich Mixed-Halide Perovskites Applied as Mesoscopic Solar Cells with a Carbon Counter Electrode. *ACS Energy Lett*. **2016**, *1*, 1086–1093.

21. Rajagopal, A.; Liang, P.-W.; Chueh, C.-C.; Yang, Z.; Jen, A. K.-Y. Defect Passivation via a Graded Fullerene Heterojunction in Low-Bandgap Pb−Sn Binary Perovskite Photovoltaics. *ACS Energy Lett*. **2017**, *2*, 2531−2539.

22. Igual-Munoz, A. M.; Ávila, J.; Boix, P. P.; Bolink, H. J. FAPb$_{0.5}$Sn$_{0.5}$I$_3$: A Narrow Bandgap Perovskite Synthesized through Evaporation Methods for Solar Cell Applications. *Sol. RRL* **2020**, *4*, 1900283.

23. Chen, Q.; Luo, J.; He, R.; Lai, H.; Ren, S.; Jiang, Y.; Wan, Z.; Wang, W.; Hao, X.; Wang, Y.; Zhang, J.; Constantinou, I.; Wang, C.; Wu, L.; Fu, F.; Zhao, D. Unveiling Roles of Tin Fluoride Additives in High-Efficiency Low-Bandgap Mixed Tin-Lead Perovskite Solar Cells. *Adv. Energy Mater*. **2021**, *11*, 2101045.

24. Savill, K. J.; Ulatowski, A. M.; Farrar, M. D.; Johnston, M. B.; Snaith, H. J.; Herz, L. M. Impact of Tin Fluoride Additive on the Properties of Mixed Tin-Lead Iodide Perovskite Semiconductors. *Adv. Funct. Mater*. **2020**, *30*, 2005594.

25. Pascual, J.; Flatken, M.; Félix, R.; Li, G.; Turren-Cruz, S.-H.; Aldamasy, M. H.; Hartmann, C.; Li, M.; Girolamo, D. D.; Nasti, G.; Hgsam, E.; Wilks, R. G.; Dallmann, A.; Bär, M.; Hoell, A.; Abate, A. Fluoride Chemistry in Tin Halide Perovskites. *Angew. Chem. Int. Ed*. **2021**, *60*, 21583 – 21591.

26. Chung, J.; Shin, S. S.; Hwang, K.; Kim, G.; Kim, K. W.; Lee, D. S.; Kim, W.; Ma, B. S.; Kim, Y.-K.; Kim, T.-S.; Seo, J. Record-efficiency flexible perovskite solar cell and module enabled by a porous-planar structure as an electron transport layer. *Energy Environ. Sci*., **2020**, *13*, 4854-4861.